1 **The catastrophic landfill flowslide at Hongao dumpsite on December 20, 2015 in Shenzhen, China**

2 Qiang Xu[1], Dalei Peng[1], Weile Li[1], Xiujun Dong[1], Wei Hu[1], Minggao Tang[1], Fangzhou Liu[2*]

3 [1]State Key Laboratory of Geohazard Prevention and Geoenvironment Protection, Chengdu University of
4 Technology, Chengdu 610059, China
5 [2]School of Civil and Environmental Engineering, Georgia Institute of Technology, Atlanta, GA, USA

6 **Abstract** A catastrophic flowslide occurred at Hongao dumpsite on Dec 20, 2015 in the Guangming New
7 District of Shenzhen, China. The flowslide caused 69 causalities with 8 missing and damaged 33 buildings.
8 In the absence of extreme weather condition and seismic activity, the cause(s) of the failure was analyzed
9 on the basis of multi-temporal remote sensing images, site investigation, *in-situ* tests, laboratory tests, and
10 numerical analyses. The preliminary results showed that the volume of the flowslide deposit was 2.32×10^6
11 m^3 and the volume of dumpsite filling was 6.27×10^6 m^3 at the time of the event, which is three times larger
12 than the design capacity. The flowslide has the characteristics of high travel velocity and long run-out
13 distance. The displaced material was primarily silty soil in mixture of construction and demolition waste at
14 high moisture content. The primary causes of the failure were concluded as follow: (1) The dumpsite
15 stagnated groundwater flow in the study area, which resulted in the saturation of the waste filling and high
16 pore water pressure due to malfunctioned drainage system and the underlying impermeable granite stratum;
17 (2) The accumulation rate and total volume of the waste filling was in exceedance of the design capacity.
18 The failure may be ascribed to the presence of excess pore water pressure as evidences of liquefaction were
19 observed at several locations, and it is postulated that such phenomena was related to the surcharge loads
20 imposed by the unregulated disposal activities.

21 **Keywords** Flowslide, Landslide, Municipal Solid Waste (MSW), Dumpsite, Landfill

22 **1 Introduction**

23 Owing to the population growth and industrialization, rapid increase in the accumulation rate of municipal
24 solid waste (MSW) poses challenges in MSW management and urban planning (Huang and Cheng, 2016).
25 Landfilling is the most common method of MSW disposal (Brunner and Fellner, 2007). Transformation of
26 an abandoned quarry to a MSW dumpsite is a general approach as it conserves resources by reclaiming the
27 quarry space and provides MSW storage solution (Zou, 2016). The landfill slope stability is critical in MSW
28 management, and thus the selection and design of landfills require engineering assessment on both slope
29 stability and environment impact.

30 The porosity and moisture content of MSW is typically high in an unregulated landfill because of inadequate
31 drainage system, and thus the failure of a MSW may exhibit fluid flow behave, i.e. flowslide, with extremely
32 high mobility (Dai et al., 2016; Huang and Cheng, 2016). Landfill slope failure in MSW dumpsite can be
33 found in previous studies, wherein 6 reported cases between 1993 and 2005 had resulted in approximately
34 500 deaths and significant economic loss (Blight, 2008; Blight and Fourie, 2005; Eid et al., 2000; Kjeldsen
35 and Fischer, 1995; Kocasoy and Curi, 1995; Merry et al., 2005; Mitchell et al., 1990). The deadliest event
36 in history killed 278 people in Manila, Philippines in 2000, and the second deadliest event buried 71 houses
37 and killed 143 people on Feb 21, 2005 at Leuwigajah dumpsite near Bandung, Indonesia (Lavigne et al.,
38 2014).

39 Shear strength of MSW is a function of various parameters, including waste type and composition, disposal
40 rate, moisture content, surcharge, and compaction (Eid et al., 2000; Huvaj-Sarihan and Stark, 2008). The
41 movement of waste failure are complex and still poorly known due to the lack of field monitoring data. The
42 existing studies have focused on empirical methods (e.g. Blight and Fourie 2005; Srour 2011), laboratory
43 experiment, and numerical analyses. An approach was presented to estimate the maximum flow velocity of
44 MSW slope failure based on energy balance (Blight and Fourie, 2005). The empirical-statistical method
45 still has widespread use in practical applications, but the accuracy is commonly model dependent (Dai et
46 al., 2016; Huang and Cheng, 2016). The mixture of peat, kaolinite, and quartz sand were used in laboratory
47 tests to study the interplay between moisture content of filling and failure in MSW landslide (Dai et al.,

48 2016). With increased moisture content of the MSW, the mobility increases while the maximum and final
49 flow depth decrease. Numerical simulation are widely used in the landfill slope stability analysis (Chang,
50 2002, 2005; Chugh et al., 2007; Huang and Cheng, 2016), where some of the more advanced methods were
51 employed such as the smoothed Particle Hydrodynamics (SPH) method for run-out distance analysis of two
52 typical landfill flow slides occurred in Sarajevo and Bandung (Huang et al., 2013).

53 A MSW landfill consists of mainly construction and demolition waste failed at the Hongao dumpsite in the
54 Guangming New District of Shenzhen, China at approximately 11:40 AM on Dec 20, 2015. The failure
55 destroyed 33 buildings and accommodations in the industrial park, and resulted in 69 causalities with 8
56 missing as of Jan 12, 2016. No extreme weather conditions or seismic activity were reported at the time of
57 the event. This article investigates the characteristics and causes of failure. Field investigation, *in-situ* tests,
58 Unmanned Aerial Vehicle (UAV) stereo-measurements, and remote sensing images were used to analyze
59 the characteristics and material properties of the slope failure. Laboratory tests and numerical analysis were
60 performed to better understand the failure mechanism.

61 **2 Data and Methodology**

62 **2.1 Satellite Image, Topographic Map, and Aerial Photo**

63 A series of satellite images of the site was obtained from Google Earth between Nov 2002 and Feb 2016.
64 Two high resolution pre-/post-failure images were acquired by satellite image and aerial photo. Topography
65 map of the pre-disposal site was provided by the local government, of which the design was submitted by
66 a third-party consulting firm in Dec 2013. Based on the project report, the design capacity was 2×10^6 m^3
67 with 9 slope benches at an average ratio of 1:2.5. The Digital Orthoimage Map (DOM) and Digital Surface
68 Model (DSM) were reconstructed from aerial photos, and a topographic map for the post-sliding dumpsite
69 was generated from the DSM at the scale of 1:1000. Structured terrain for vehicles was excavated before
70 failure which consisted of 9 benches and 3 platforms. Topographic map for the pre-sliding dumpsite was
71 derived by combining the images of the original, pre-sliding, and post-sliding slopes, which also provided
72 an estimation on the volume and depth of the pre-/post-sliding landfill.

73 **2.2 Field Investigation and *in-situ* Tests**

74 The initial field investigation was conducted on Dec 23, 2015, with a follow-up field investigation on Jan
75 21-25, 2016. Field investigations assessed the topographical, geological, and groundwater conditions. The
76 density, moisture content, and permeability of the displaced material of the flowside was measured *in-situ*.

77 **2.3 Laboratory Tests and Numerical Analysis**

78 Undisturbed and reconstituted soil samples were used for laboratory tests, including weathered silty soil
79 and waste fillings. Grain size distribution was conducted using wet sieve analysis. Maximum dry density
80 and optimum moisture content of the displaced material were determined by standard compaction test. The
81 shear parameters of the displaced material (c and ϕ) were obtained by triaxial compression test. In order to
82 analyze the stability of the dumpsite, input parameters for the material properties and model geometry were
83 the same as the corresponding values measured on site or in the laboratory. Mobilized shear strength was
84 back-analyzed using conventional limit equilibrium method (LEM) to demonstrate the complexity of such
85 progressive failure involving liquefaction and post-failure landslide propagation.

86 **3 Geological and Climatic Setting**

87 The location of the site is shown in Fig. 1a, of which the pre-failure image was obtained by Pleiades image
88 on Dec 18, 2015 (2 days before failure) and the post-failure aerial image was taken by UAV (3 days after
89 failure) as shown in Fig. 1b and 1c, respectively. The dumpsite was located at 23 km away from Shenzhen
90 and 5 km away from the Guangming New District (E113°56'5", N22°42'44"). The dumpsite was surrounded
91 by three ridges with a free face excavated with a mild slope gradient. The bedrock of the dumpsite is mainly
92 Cretaceous granite rock (Fig. 2a and 2b). The landfill consisted of construction waste with silty soil, clay,
93 rock, and gravel (Fig. 2 and 3).
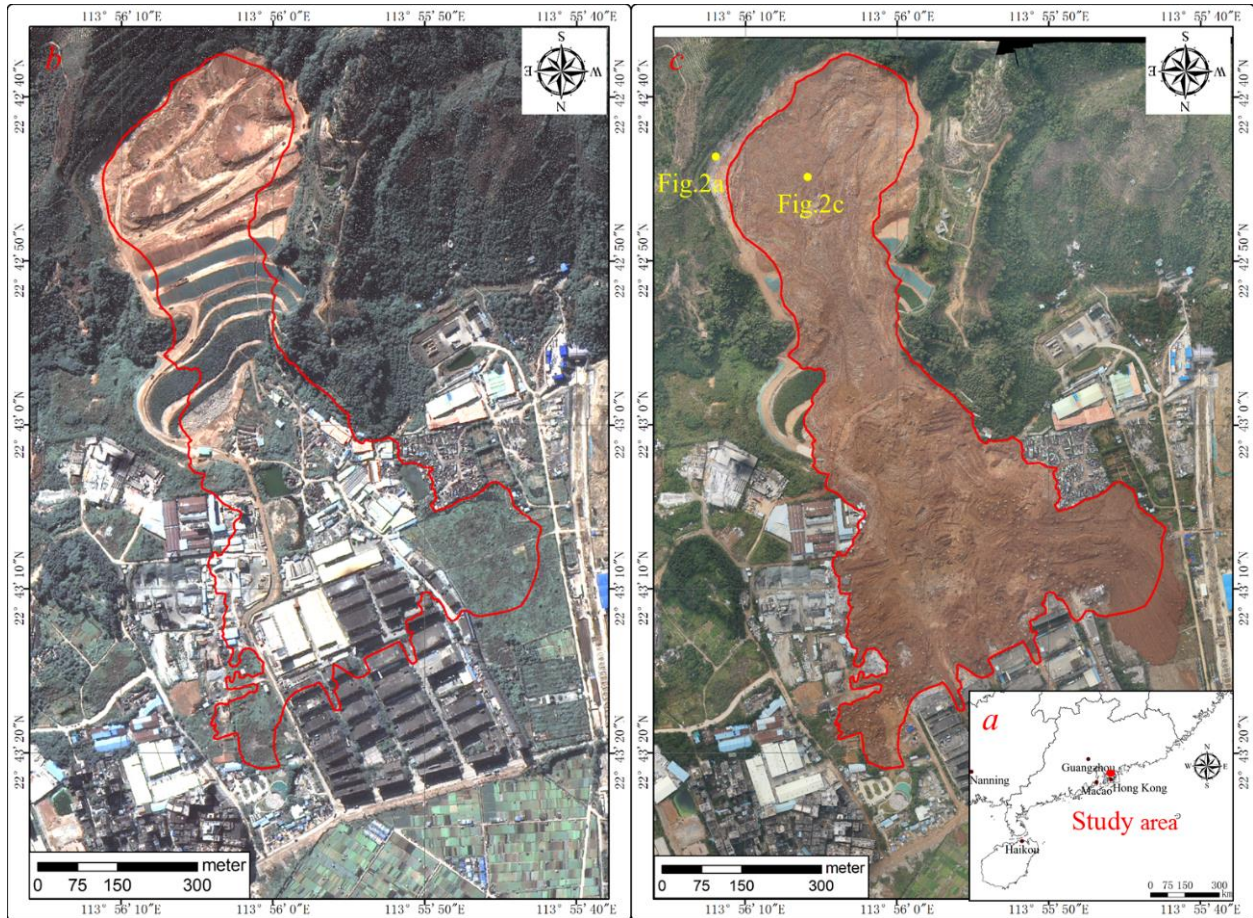
Fig. 1 Location of the study site and images of the pre-/post-failure dumpsite. The boundary of the flowslide is indicated in red. **a** the location of the study area; **b** Pleiades satellite image (Dec 18, 2015); **c** Aerial photo of the flowslide (Dec 23, 2015).

The study area belongs to the zone of subtropical monsoon climate with an average temperature of 22° and an average annual precipitation of 1500 mm concentrating between April and September (greater than 85 % of the annual precipitation) (Zhang et al., 2006). Based on the rainfall data from the nearby Tangjia Rainfall Station between Jan 1, 2013 and Dec 20, 2015 (Fig. 4), the accumulated precipitation in the study area was nearly 3240 mm. The catchment area of the study area was $4.7 \times 10^5 \, m^2$, which was 2.95 times greater than the area of the dumpsite ($1.6 \times 10^5 \, m^2$) as shown in Fig. 5a. Drainage system was implemented in the study area, where surface run-off was designed to be collected by the drainage pipes installed at a higher elevation above the dumpsite and diverted into the peripheral drainage channel. Field evidences suggested that the drainage system was abandoned (Fig. 5b and 5c), possibly in the lack of maintenance. With the inadequate drainage, the ingress of rainwater in the dumpsite was permitted (Fig. 6c), in addition to the concentration of surface run-off and groundwater into the dumpsite. Field test estimated that the permeability of the waste filling was 5.26×10^{-6} cm/s. Low permeability and inadequate drainage resulted in the high moisture content and high pore water pressure in the dumpsite. The groundwater in the area were mainly bedrock fissure water and Quaternary pore water (Fig. 6).

112

113 Fig. 2 Photos of the rock and soil specimen collected from the displaced material. **a** Exposed granite rock
114 near the flowslide scarp; **b** Close view of the granite rocks; **c** Displaced material in the zone of depletion;
115 **d** Materials in the flowslide source area.
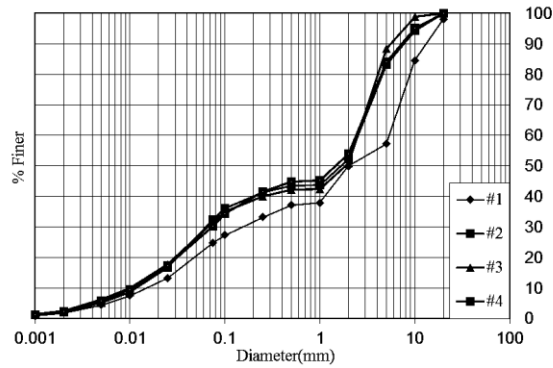
116

117 Fig. 3 Particle size distribution of the waste filling (with sieve sizes of 20, 10, 5, 2.0, 1, 0.5, 0.25, 0.10,
118 0.075, 0.025, 0.01, 0.005, 0.002, and 0.001 mm)
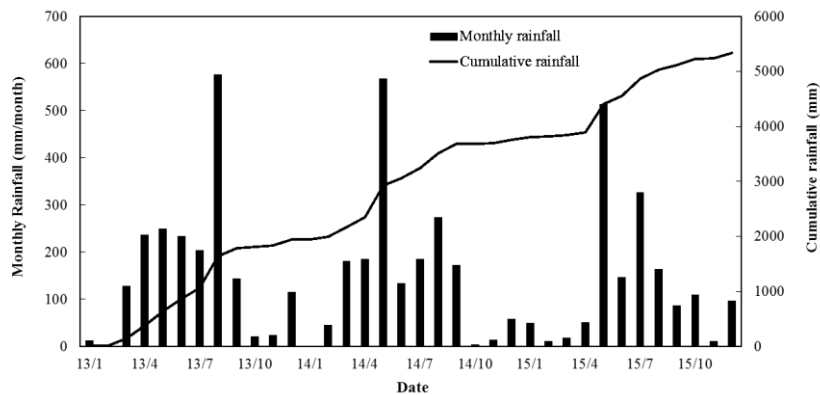
119

120 Fig. 4 Monthly rainfall and cumulative precipitation between 2013 and Dec 2015.

121

122 Fig. 5 **a** An overview of the catchment area (Google Earth image); **b** The surrounding peripheral drainage
123 channel of the dumpsite was abandoned; **c** Damaged drainage pipes were not repaired and failed to divert
124 surface run-off into the peripheral drainage channel. Surface run-off concentrated in the waste filling.
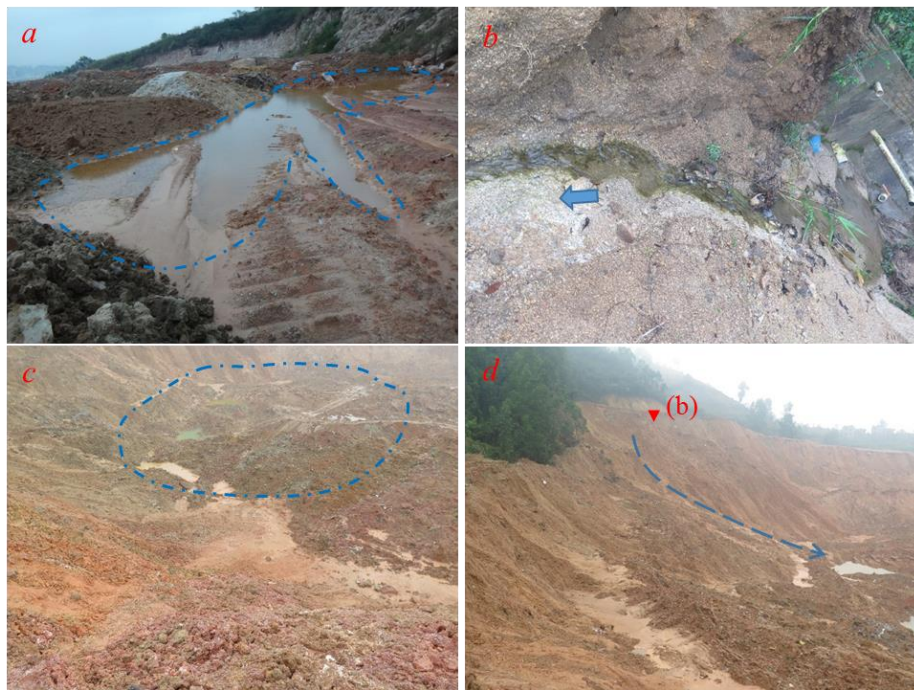
125

126 Fig. 6 **a** Groundwater overflow in the rock fissures near the flowslide crown; **b** Water accumulation in the
127 flowslide crown; **c** Water accumulation in the source area; **d** Surface run-off and infiltration contributed to
128 groundwater seepage.

4 Multi-Temporal Remote Sensing Images

The development of dumpsite and landform changes are presented by a series remote sensing images taken between 2002 and 2016 (Fig. 7). It is postulated that the quarry was active between 2002 and 2008. However, formation of ponds of various sizes at different spatial and temporal locations in the quarry indicated low permeability and the lack of drainage network (Fig. 7b, 7c, and 7d). The quarry was abandoned in or before 2008 as shown in Fig. 7c (Feb 20, 2008) with a small amount of waste filling in the pit. A large-scale pond was later formed due to groundwater and rainfall accumulation (Fig. 7d). The depth of the pit was over 100 m before the systematic disposal activities. A service road was excavated between two rock hills exiting the quarry and formed a small-scale gully cross the pit longitudinally (Fig. 7a, 7b, 7c, and 7d). Additionally, a small-scale platform (office area of the abandoned quarry) was excavated at immediate downstream of the quarry exit. The gully was covered during the construction of a multi-bench retaining slope between the rock hills as waste disposal continued throughout the process (Fig. 7e). Disposal activity started possibly in 2014 (Fig. 7e and 7f), and the accumulation rate of the waste filling was considerably fast (Zou, 2016).

An unpaved road was excavated on the east of the quarry connecting the crest and toe of the hillslope as shown in Fig. 7e. A large number of trucks can be seen transporting waste filling to the dumpsite. A large amount of construction waste was dumped in the pit with 4 slope benches built at the exit of the pit (Fig. 7e). The volume of the waste increased significantly with the 1st and 2nd benches completed in late 2014, and the 3rd to 4th benches were still under construction until Jan 2015 (Fig. 7f).

The rapid accumulation and the total volume of the waste filling received some attentions before failure. An environmental assessment provided by a third-party consulting firm warned the erosion at the site and its influence on the slope stability in Jan 2015 (Zou, 2016). The disposal activity was ceased for a while as no trucks were seen in the image (Fig. 7f), and it was verified by the interview with the local inhabitants. The disposal activity was resumed in or before April 2015, and the 4th bench was completed by then (Fig. 7g). By comparing Fig. 7g and Fig. 7h, significant modifications on the landform occurred with a major increase in the volume of the waste filling as the landfill was close to the crest of the pit. The waste filling appeared flattened and disposal activity was intense as more than 20 trucks were found in Fig. 7h. A total of 8 slope benches were completed with surface drainage channels installed on the hillslope, and the 9th bench was still under construction before failure. The thickness of the waste filling was around 90 m with a volume of $6.3 \times 10^6 \, \text{m}^3$ (Fig. 8a) by extracting the difference between the pre- and post-filling DEMs.

158
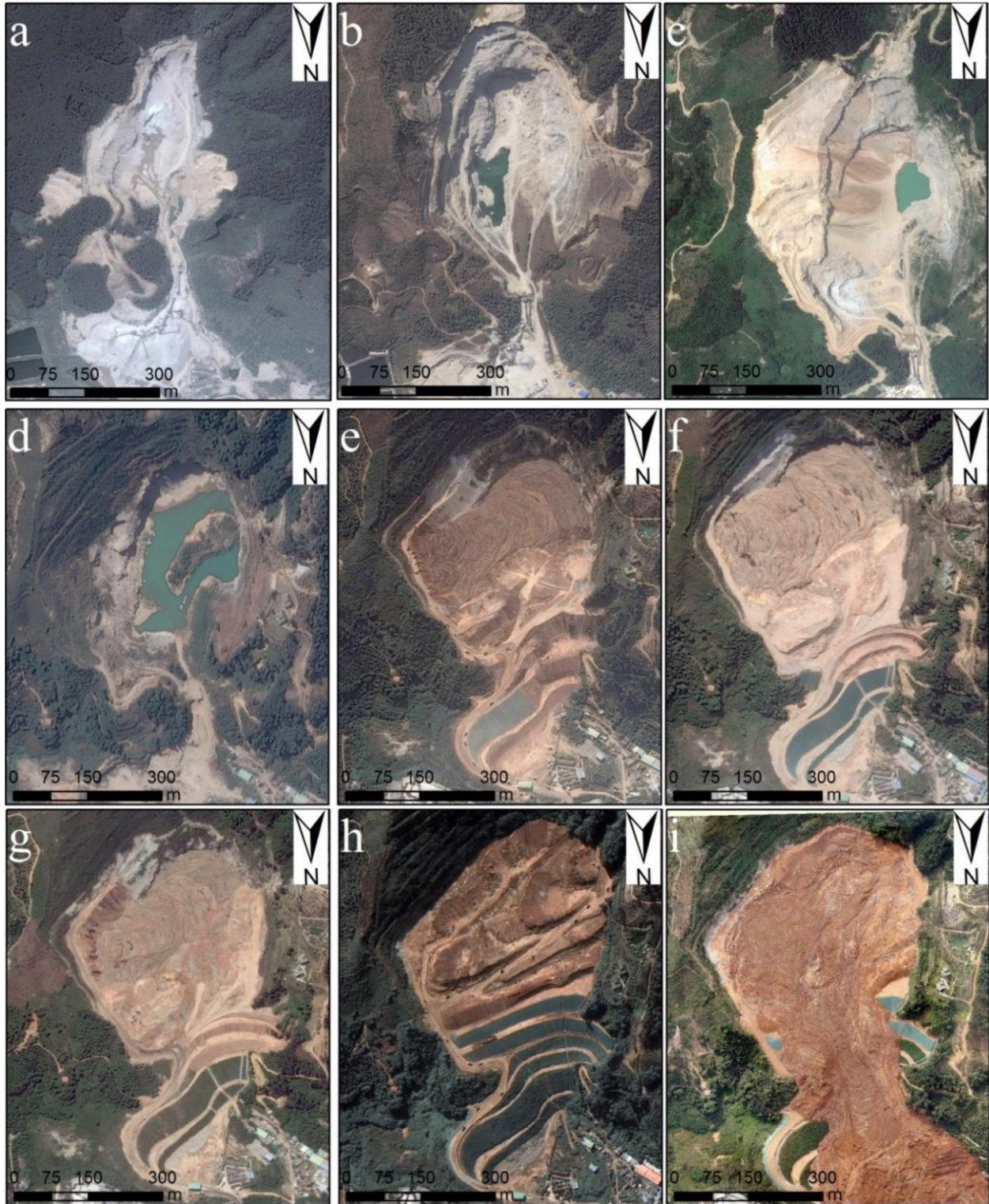
Fig. 7 Multi-temporal remote sensing images of the study area. **a** 08/31/2002; **b** 02/20/2008; **c** 08/30/2010;
d 11/25/2013; **e** 11/17/2014; **f** 01/23/2015; **g** 04/14/2015; **h** Pleiades (12/18/2015); **f** Aerial (12/23/2015).
Image **a** to **g** were obtained from Google Earth. A service road was excavated at the exit of the quarry with
a width of nearly 70 m (see image **a**, **b**, **c**, and **d**).
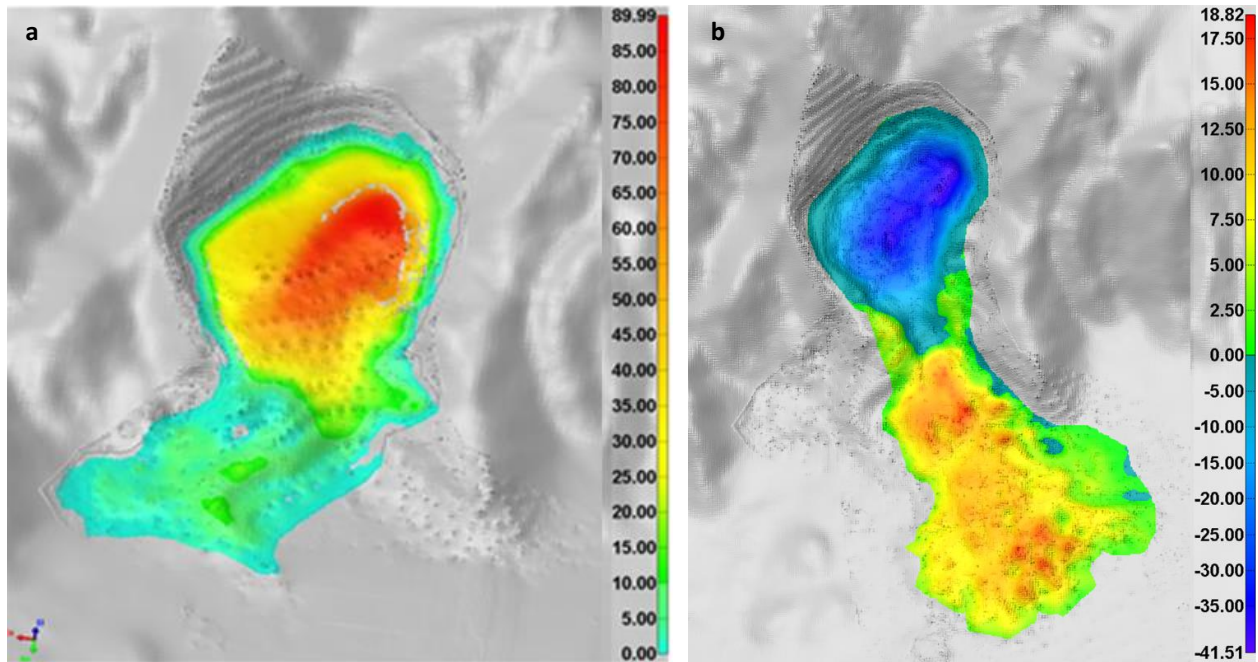
164 Fig. 8 **a** The thickness distribution of the dumpsite based on the pre-/post-disposal DEMs; **b** The elevation
165 variations of the dumpsite estimated between the pre-/post-sliding DEMs.

5 Flowslide Characteristics

167 The flowslide area can be divided into the source area and flow-accumulation area as shown in Fig. 9. The
168 source area was the abandoned quarry pit. The mass slid in the direction of 340° with maximum traveling
169 distance of 1203 m. The maximum thickness of the remaining material in the source area was 41.51 m with
170 an average of 20.5 m (Fig. 9 and Fig. 10). The maximum deposit thickness in the flow-accumulation area
171 was 18.2 m with an average of 8.21 m (Fig. 8b). The geometry of a flowslide can be expressed in length
172 (L), height (H), width (W), and area (S) (Legros, 2002; Scheidegger, 1973). The geometric parameters are
173 indicated in the simplified flowslide geometry in Fig. 11 with values listed in Table 1, Table 2 and Table 3.
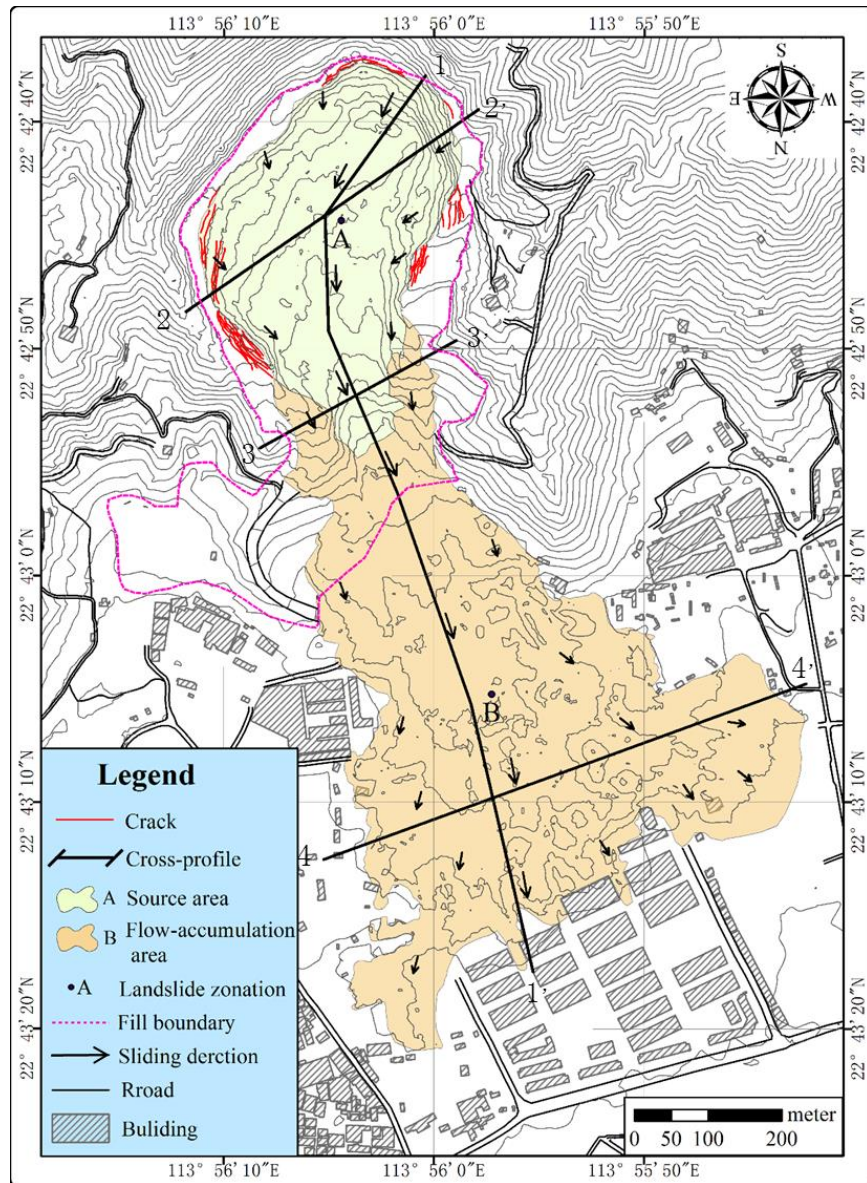
174
175 Fig. 9 The topographic map of the flowslide.
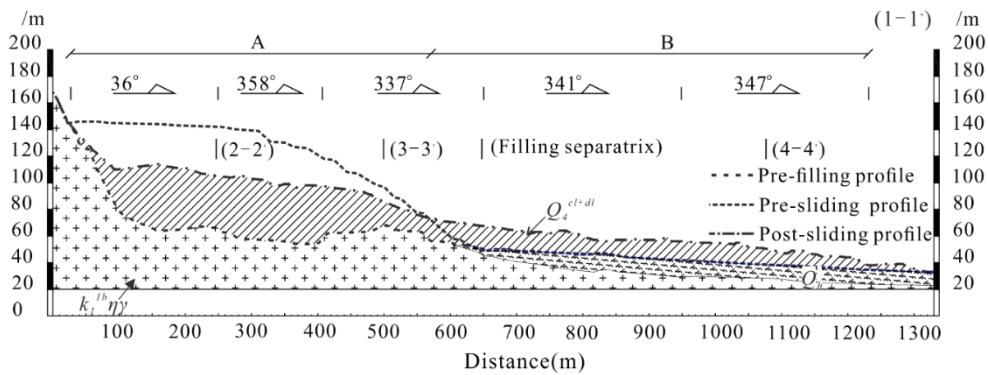
176
177 Fig. 10 The geological and topographical cross section (profile line 1-1')
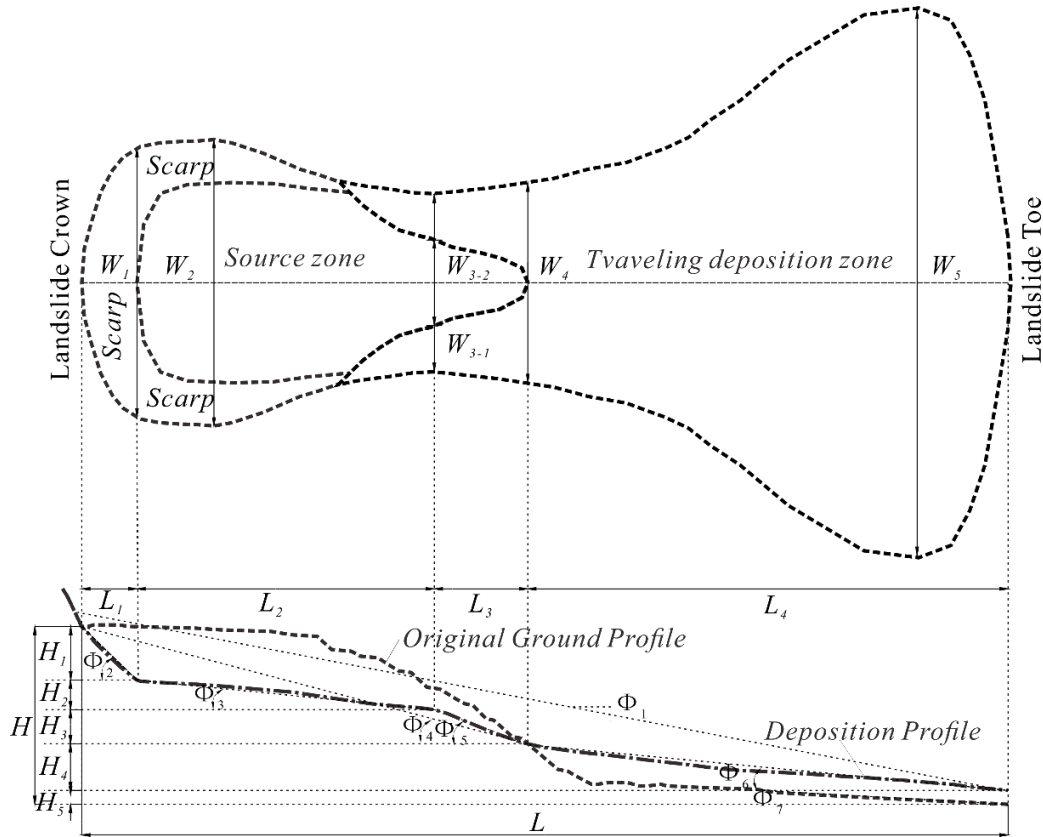
178

179 Fig. 11 Simplified illustration of the flowslide geometry. L: run-out distance; H: elevation; W_1: scarp width;
180 W_2: max width of the source area; W_3: frontal width of the source area; W_4: width of the shear crack; W_5:
181 max width of the flow-accumulation area; L_1: horizontal length of the scarp; L_2: horizontal length of the
182 mild slope; L_3: horizontal length of the steep slope; L_4: horizontal length of the flow-accumulation area; H_1:
183 height of the scarp; H_2: height of the mild slope; H_3: height of the steep slope; H_4: height of the flow-
184 accumulation area; H_5: thickness of the toe of the flowslide; Φ_1: extension angle; Φ_2: slope gradient of the
185 scarp; Φ_3: mild slope gradient; Φ_4: slope gradient of the source area; Φ_5: steep slope gradient; Φ_6: slope
186 gradient of the flow-accumulation area; Φ_7: slope gradient of the foundation area

187

Table 1 Geometric parameters of the flowslide (Length and Width)

Parameter	L (m)	H (m)	W_1 (m)	W_2 (m)	W_{3-1} (m)	W_{3-2} (m)	W_{4-1} (m)	W_{4-2} (m)	W_5 (m)
Value	1204.67	111.31	212.5	399.32	218.31	149.38	217.71	64.63	592.25

188

Table 2 Geometric parameters of the flowslide (Angle)

Parameter	Φ_1 (°)	Φ_2 (°)	Φ_3 (°)	Φ_4 (°)	Φ_5 (°)	Φ_6 (°)	Φ_7 (°)	K	S (m²)
Value	5.28	28.06	1.2	7.62	11.36	3.08	1.36	0.32	398619.6

189

Table 3 Geometric parameters of the flowslide (Area and Thickness)

Parameter	Area A	Area B
S (m²)	11.35×10^4	28.51×10^4
V (m³)	2.32×10^6	2.34×10^6
T_{max} (m)	41.51	18.82
T_{ave} (m)	20.49	8.21

5.1 Source Area

The source area of the flowslide is the quarry pit with a length (L_{1+2+3}) of 540.30 m and a width (W_2) of 399.32 m. The area of the source area (S_A) is 11.35×10^4 m^2 and the height (H_{1+2+3}) was 68.5 m with an apparent dip (Φ_4) of 7.62° (Fig. 12 and Table 1). The volume of the mobilized material from the source area was 2.32×10^6 m^3 and the remaining volume was 3.95×10^6 m^3. The maximum thickness of the source area (T_{A-max}) was 41.5 m with an average thickness (T_{A-ave}) of 20.5 m. The west of the main scarp has steep slope gradient with mild gradient on the east. The height of the steep scarp ranged 25-47 m, while the height of the mild scarp ranged 10-20 m. The geological cross section (profile line 2-2') is shown in Fig. 12c. The maximum thickness of the source area was 40.65 m with an average of 34.83 m. The overview of the source area and surface cracks are shown in Fig. 12a and 12b, respectively.
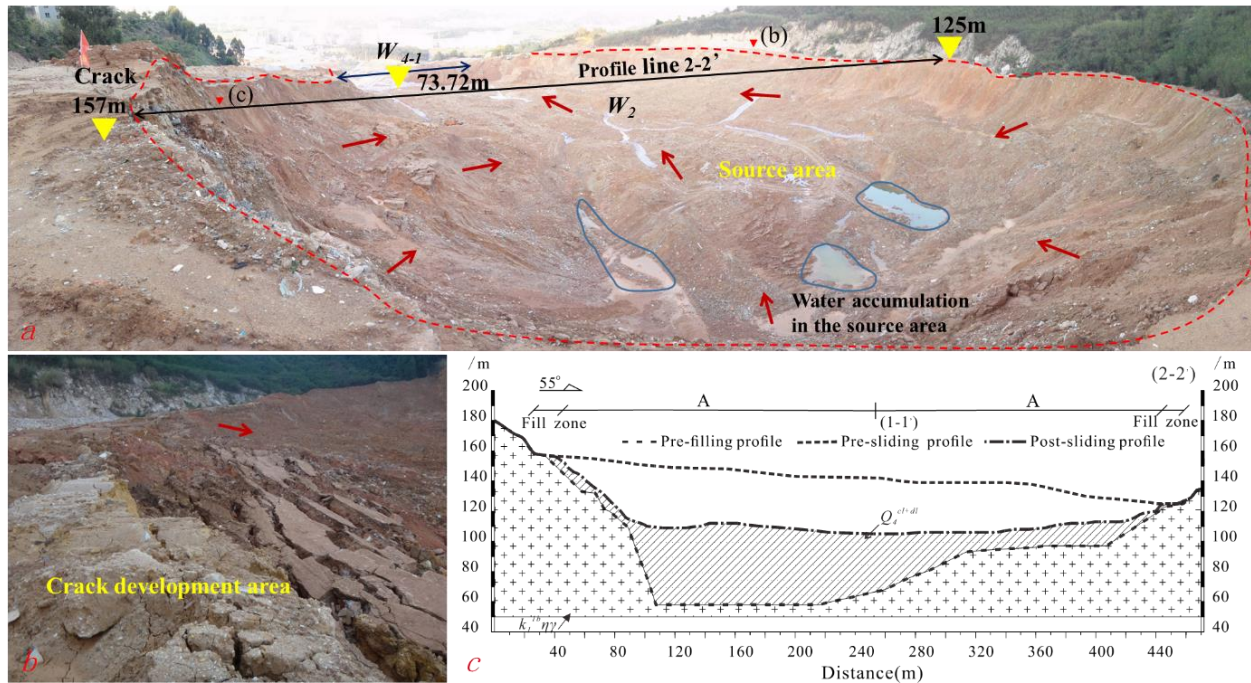
Fig. 12 **a** An overview of the source area (image taken at the flowslide crown facing north). A large opening (W_{4-1}) formed due to the failure of the retaining slope (the exit of the original quarry pit), which provided passage for the flowslide and permitted rapid release of kinematic energy; **b** Surface cracks were developed due to unloading near the crest and the flanks of the flowslide; **c** The geological cross section (profile line 2-2') of the source area.

With the ingress of rainwater and groundwater in the dumpsite, pore water pressure increases due to low permeability of the underlying granite. The lack of drainage resulted in waste filling saturation in the basal zone of the dumpsite which appeared as the final sliding bed of the flowslide (Fig. 12a).

A large amount of silty soil were observed in the source area. The material on both sides of the source area were mobilized due to the debuttressing effect as the waste filling in the lower portion of the dumpsite slid into the downstream industrial park, and in consequence, caused further collapse of the dumpsite. Step-like steep scarp was formed on the west of the main scarp with tensile cracks developed on the rear edge as well as both sides of the scarp.

The presence of the aforementioned rock hills formed unfavorable topography for retaining slope stability by promoting a narrow gully for groundwater flow (Fig. 7c and Fig. 9). As a result of the retaining slope failure, a large opening was formed at the elevation of 73.7 m (between the front edge of the steep scarp and the rear edge of the flow-accumulation area) as shown in Fig. 9, Fig. 10, and Fig. 12a. The displaced material was stratified in the middle part of the flow-accumulation area during the high-speed sliding. The

shape of the failed retaining slope was half-elliptic-like with a width (W_{4-1}) of 217.7 m and a height (H_b) of 27.5 m (Fig. 13a and 13c).
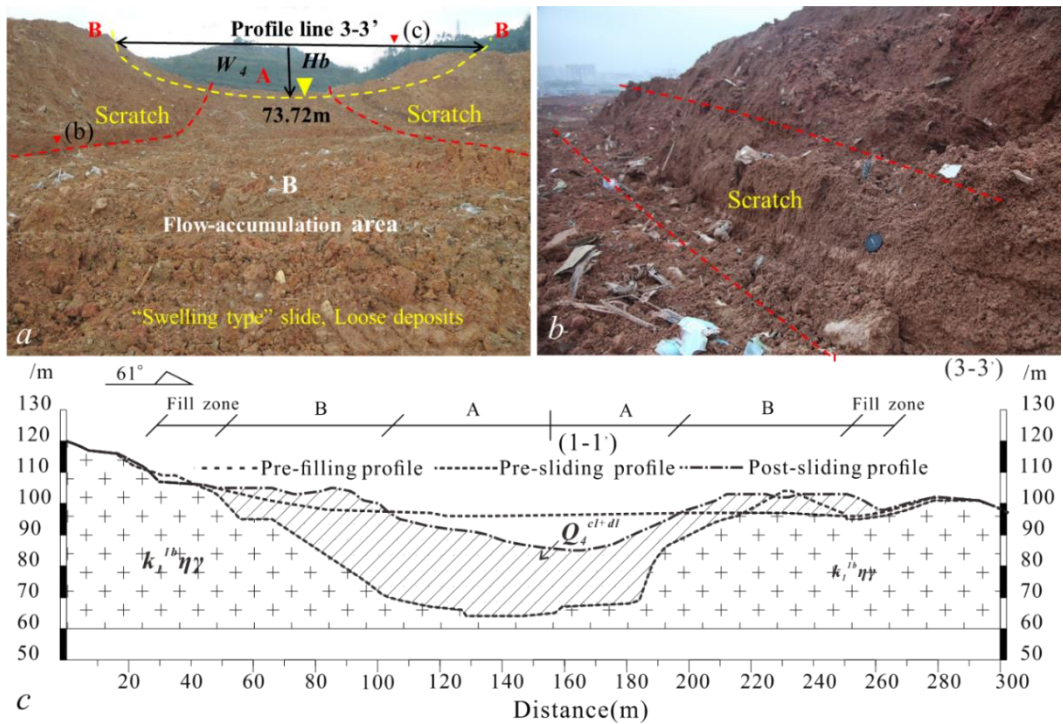
Fig. 13 **a** The half-elliptic-like opening of the failed retaining slope; **b** Details on the scratch caused by the mass movement; **c** Geological cross section (profile line 3-3') of the failed retaining slope located at the original quarry pit between the two rock hills.

5.2 Flow-Accumulation Area

The fan-shaped flow-accumulation area mantled the retaining slope of the dumpsite and a large part of the industrial park as shown in Fig. 12a. The original slope gradient of the industrial park (Φ) was 1.36° along the profile line 1-1' as shown in Fig. 12 and Table 1. The area located immediately downstream of the dumpsite was relatively flat with no major construction except a pond (area approx. 3600 m²) and a channel (width: 7 m and length: 130 m). Most of the industrial structures were constructed on east, west, and north side of the pond as shown in Fig. 9, and thus created a ideal flow channel for the flowslide. The failure of the rock retaining slope resulted in an opening for the waste fill movement which subsequently destroyed downstream buildings (Fig. 14 and 15).

234
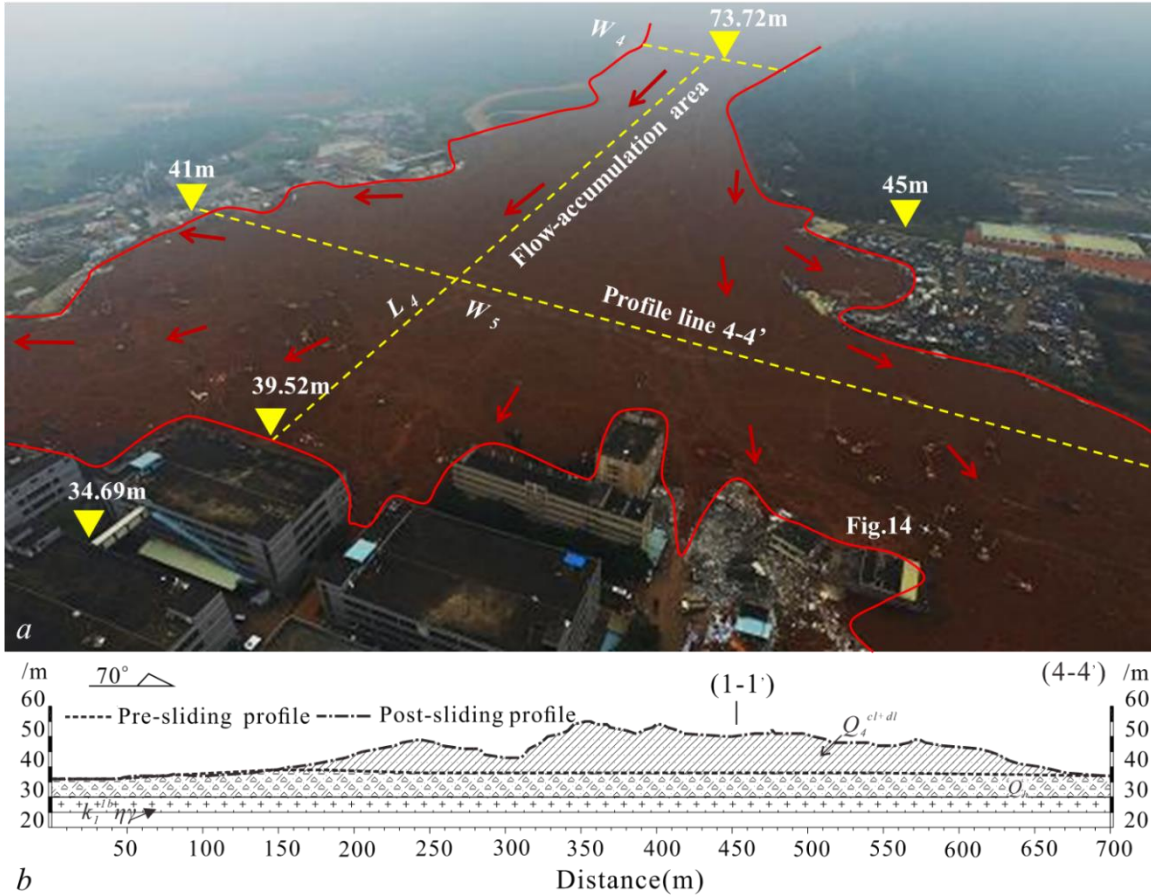
235 Fig. 14 **a** The overview of the flow-accumulation area with elevations (China News Agency); **b** Geological
236 cross section (profile line 4-4') of the flow-accumulation area. The length (L_4) was 664.4 m and the width
237 (W_3) was 218.3 m with the width of the front edge (W_5) of 592.3 m. The area of the flow-accumulation area
238 is 28.51×10^4 m^2, and the elevation difference (H_4) was 35.7 m with an apparent dip (Φ_6) of 3.08°. The
239 average thickness in the flow-accumulation area was 8.21 m with the maximum thickness of 18.82 m (Fig.
240 12c, Table 1, and Table 3).

241
242 Fig. 15 The damage of buildings in the industrial park (China News Agency)

6 Back-Analyses of the Flowslide

6.1 Flowslide Movement

The high sliding velocity and long-runout distance of the flowslide may be related to a more diffuse failure due to liquefaction near the base of the slope. Evidences of localized liquefaction can be found at several locations (Fig. 16). Empirical correlation was used to back-calculate the flowslide travel velocity on the basis of its geometrical characteristics. To better understand the failure mechanism, laboratory tests and numerical analyses were performed.

Fig. 16 Evidences of liquefaction near the opening of the failed slope.

The source area of the flowslide was in the elevation of 142 m and the horizontal run-out distance (L) was approximately 1203 m with an elevation difference (H) of 111 m. The velocity of a high-speed landslide can be estimated by $v = \sqrt{2g \times (H - f \times L)}$ (Scheidegger, 1973), where v is the sliding velocity (m/s), g is the gravitational acceleration (m/s^2), H and L are the elevation difference and horizontal distance (m) between the crown and toe of the flowslide, respectively. f is the equivalent friction coefficient referred as the ratio of height and run-out distance of the flowslide ($f = $ H/L). The equivalent friction coefficient of the dumpsite flowslide was 0.092. The relations of run-out distance, elevation difference, and equivalent friction coefficient were defined by the flowslide geometry as shown in Fig. 11. The sliding velocity was back-calculated and presented in Fig. 17.
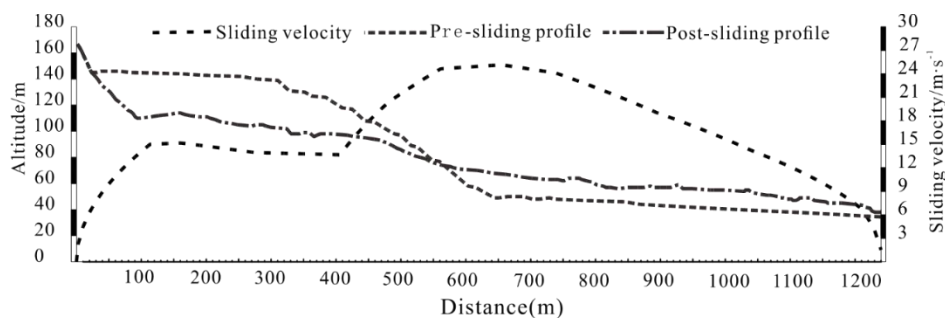
Fig. 17 The relationship between sliding velocity along profile line 1-1' and pre-/post-sliding landform.

Based on the back-calculated velocity profile, two sharp increases were identified, including the initiation of the waste filling near the steep scarp and the acceleration of the flowslide when exiting the dumpsite. The sliding velocity was increased to 15.17 m/s as waste filling reached the bottom of the steep scarp. The velocity displaced material gradually decreased to approximately 13 m/s before accelerate to the maximum velocity of 25.15 m/s as it reached the opening of the quarry. The second sharp acceleration was followed by the rapid dissipation of kinematic energy and reduction in velocity after reaching the flow-accumulation area (elev. 50 m). It was estimated that the sliding velocity was reduced to 15.68 m/s when it made contact

270 with the downstream buildings, and then ceased moving due to the obstruction. The geometry and velocity
271 exhibited clear characteristics associated with high-speed long-runout flowslides.

272 **6.2 Numerical Analyses**

273 Basic material properties were obtained from *in-situ* and laboratory tests. Dry density of the waste filling
274 was 1.25-1.48 g/cm^3 with a void ratio of 0.83-1.31. Standard compaction tests suggested that the optimal
275 water content of 15.31% with highest dry density of 1.79 g/cm^3. The surface of the filling was in loose state
276 with the degree of compaction of 69.83%-82.68%. Based on the undrained shear test, the c and ϕ of the
277 filling were 4.7 kPa and 31.9°, respectively, and thus the friction angle was considerably higher than the
278 gradient of the slope. No strain-softening was observed in the saturated specimen under triaxial tests.

279 Numerical simulation for diffuse failure involves liquefaction and post-failure propagation is challenging
280 (Take and Beddoe, 2014), and the conventional LEB is typically not applicable for analyzing propagation
281 of landslide originating from diffuse failure induced by liquefaction (Cascini et al., 2009, 2013). Back-
282 analyses was performed using SLOPE/W with Morgenstern Prince Limit Equilibrium Analysis under the
283 assumption of a fully saturated basal zone in the dumpsite before failure. The back-analyses using LEB
284 method typically set the FoS to unity for back-calculating the mobilized strength. The final sliding surface
285 and a hypothetic groundwater level were added to determine the shear strength in an iterative approach with
286 estimated dry density of filling of 1.65 g/cm^3 (Fig. 18), however the back-calculated friction angle was
287 significantly less than the experimental result.
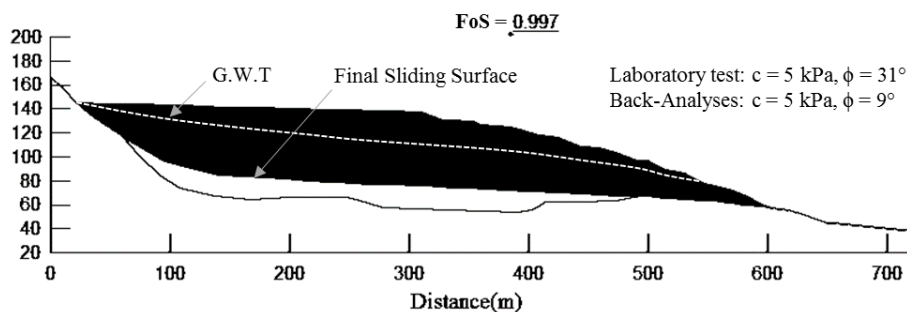
289 Fig. 18 Back-calculated mobilized strength by using 2D numerical model with LEM.

290 The implausible mobilized strength shows that back-analyses using LEB is not applicable to the flowslide,
291 as the failure may involve liquefaction with subsequent progressive failure and post-failure propagation.
292 Notwithstanding the complex progressive mechanism and over-simplified force equilibrium method, the
293 misleading results of the back-analyses can be directly ascribe to the misuse of static pre-shearing pore-
294 water pressure with measured final sliding surface. Such erroneous back-analyses strategy was discussed
295 in detail in previous study (Take and Beddoe, 2014). It was postulated that the failure initiated at a relatively
296 shallow depth near the base of the slope as a result of liquefaction, which was followed by the progressive
297 backward mobilization of the fillings in the dumpsite.

298 The exact reason(s) of excess pore water pressure remains unclear at this point, however it may involve: (1)
299 rapid surcharge on the dumpsite while pore water pressure cannot dissipate sufficiently fast, and/or (2) the
300 waste filling was loosely packed with large pores in the mesco-structure, and the collapse of the structure
301 lead to the shrinkage of pores, which resulted in the excess pore water pressure. Since the permeability of
302 the waste filling was considerably low, it likely result in saturation in the basal zone of the waste filling. As
303 no clear drainage passage were found in the filling, the displaced material may remain undrained 'at failure'.

304 **7 Conclusion**

305 The Hongao dumpsite failure is of direct interest to the scientific community due to its complex progressive
306 failure mechanism and significant societal impact. The flowslide was investigated here to better understand
307 the characteristics and mechanism of the failure. The flowslide is divided into the source area and the flow-

308 accumulation area. The volume of the source area was 2.32×10^4 m^3 with the average thickness of 20.5 m
309 (max. 41.5 m). The volume of the fan-shaped flow-accumulating area was 2.34×10^6 m^3 with the average
310 thickness of 8.2 m (max. 18.8 m). The volume expansion coefficient of the flowslide was 1.007. The
311 maximum sliding velocity of the flowslide was 25.15 m/s at the opening of the dumpsite, and reduced to
312 15.68 m/s as it reached the industrial park and ceased moving due to the obstruction of buildings.

313 The flowslide was characterized by high-speed and long run-out distance, which may be related to the (1)
314 suitable topography with a height of 124 m between the crown and toe with large potential energy needed
315 for high-speed and long run-out flowslide, and (2) the low permeability and lack of drainage in the waste
316 filling in the dumpsite with impermeable bedrock resulted in groundwater stagnation, and thus high pore-
317 water pressure. Additionally, the volume of the waste filling was estimated as 6.27×10^6 m^3, which was three
318 times larger than the design capacity of the dumpsite. The failure of the retaining slope constructed between
319 two bedrock ridges formed a narrow opening for the flowslide, which facilitated the sudden release of
320 kinematic energy generating high sliding velocity and long travel distance.

321 The failure mechanism remains unclear yet it was clear that a more diffuse failure occurred with liquefaction
322 and post-failure propagation of the flowslide. The inapplicability of the LEM demonstrated the complexity
323 of the mechanism by yield erroneous mobilized strength, which also indicates the predicament of simulating
324 liquefaction-induced slope failures with conventional numerical approaches. The cause(s) of excess pore-
325 water pressure is not clear, but the unregularly disposal activities in addition to the ingress of rainwater and
326 high pore water pressure played important roles in deformation of the dumpsite. Although the flowslide
327 destruction process was fast with excessive deposits, it is postulated that signs of deformation may have
328 already appeared in the study site but not discovered due to the absence of field monitoring. Further analysis
329 is undergoing at SKLGP to assess the cause(s) involved for generating the excess pore water pressure.

330 **Acknowledgments** Authors are indebted to Dr. J. David Frost for his constant support on the collaboration.
331 The work was financially supported by the NSFC (Grant No. 41521002) and the National State Key 973
332 Project (Grant No. 2014CB744703) from the Ministry of Science and Technology of the People's Republic
333 of China.

Reference

335 Blight, G.: Slope failures in municipal solid waste dumps and landfills: a review, Waste Manag. Res.,
336 26(5), 448–463, doi:10.1177/0734242X07087975, 2008.
337 Blight, G. E. and Fourie, A. B.: Catastrophe revisited–disastrous flow failures of mine and municipal
338 solid waste, Geotech. Geol. Eng., 23(3), 219–248, 2005.
339 Brunner, P. H. and Fellner, J.: Setting priorities for waste management strategies in developing countries,
340 Waste Manag. Res., 25(3), 234–240, doi:10.1177/0734242X07078296, 2007.
341 Cascini, L., Cuomo, S., Pastor, M. and Sorbino, G.: Modeling of rainfall-induced shallow landslides of
342 the flow-type, J. Geotech. Geoenvironmental Eng., 136(1), 85–98, 2009.
343 Cascini, L., Cuomo, S., Pastor, M. and Sacco, C.: Modelling the post-failure stage of rainfall-induced
344 landslides of the flow type, Can. Geotech. J., 50(9), 924–934, 2013.
345 Chang, M.: A 3D slope stability analysis method assuming parallel lines of intersection and differential
346 straining of block contacts, Can. Geotech. J., 39(4), 799–811, doi:10.1139/t02-020, 2002.
347 Chang, M.: Three-dimensional stability analysis of the Kettleman Hills landfill slope failure based on
348 observed sliding-block mechanism, Comput. Geotech., 32(8), 587–599, 2005.
349 Chugh, A. K., Stark, T. D. and DeJong, K. a: Reanalysis of a municipal landfill slope failure near
350 Cincinnati, Ohio, USA, Can. Geotech. J., 44(1), 33–53, doi:10.1139/t06-089, 2007.
351 Dai, Z., Huang, Y., Jiang, F. and Huang, M.: Modeling the flow behavior of a simulated municipal solid
352 waste, Bull. Eng. Geol. Environ., 75(1), 275–291, doi:10.1007/s10064-015-0735-8, 2016.
353 Eid, H. T., Stark, T. D., Evans, W. D. and Sherry, P. E.: Municipal solid waste slope failure. I: Waste and
354 foundation soil properties, J. Geotech. Geoenvironmental Eng., 126(5), 397–407, 2000.
355 Huang, Y. and Cheng, H.: A simplified analytical model for run-out prediction of flow slides in municipal

356 solid waste landfills, Landslides, 1–9, doi:10.1007/s10346-016-0688-4, 2016.
357 Huang, Y., Dai, Z., Zhang, W. and Huang, M.: SPH-based numerical simulations of flow slides in
358 municipal solid waste landfills., Waste Manag. Res., 31(3), 256–64, doi:10.1177/0734242X12470205,
359 2013.
360 Huvaj-Sarihan, N. and Stark, T. D.: Back-Analyses of Landfill Slope Failures, 6th Int. Conf. Case Hist.
361 Geotech. Eng., (2), 1–7, 2008.
362 Kjeldsen, P. and Fischer, E. V: Landfill gas migration - field investigations at Skellingsted landfill,
363 Denmark, Waste Manag. Res., 13(5), 467–484, 1995.
364 Kocasoy, G. and Curi, K.: The Ümraniye-Hekimbaşi open dump accident, Waste Manag. Res., 13(4),
365 305–314, 1995.
366 Lavigne, F., Wassmer, P., Gomez, C., Davies, T. A., Sri Hadmoko, D., Iskandarsyah, T. Y. W. M.,
367 Gaillard, J., Fort, M., Texier, P., Boun Heng, M. and Pratomo, I.: The 21 February 2005, catastrophic
368 waste avalanche at Leuwigajah dumpsite, Bandung, Indonesia, Geoenvironmental Disasters, 1(1), 1–12,
369 doi:10.1186/s40677-014-0010-5, 2014.
370 Legros, F.: The mobility of long-runout landslides, Eng. Geol., 63, 301–331 [online] Available from:
371 http://www.sciencedirect.com/science/article/pii/S0013795201000904 (Accessed 25 June 2014), 2002.
372 Merry, S. M., Kavazanjian Jr, E. and Fritz, W. U.: Reconnaissance of the July 10, 2000, Payatas landfill
373 failure, J. Perform. Constr. Facil., 19(2), 100–107, 2005.
374 Mitchell, J. K., Seed, R. B. and Seed, H. B.: Kettleman Hills waste landfill slope failure. I: Liner-system
375 properties, J. Geotech. Eng., 116(4), 647–668, doi:10.1061/(ASCE)0733-9410(1990)116:4(647), 1990.
376 Scheidegger, A. E.: On the prediction of the reach and velocity of catastrophic landslides, Rock Mech.
377 Rock Eng., 5(4), 231–236, doi:10.1007/BF01301796, 1973.
378 Srour, G.: Mine waste failure: an analysis of empirical and graphical runout prediction methods,
379 University of British Columbia., 2011.
380 Take, W. A. and Beddoe, R. A.: Base liquefaction: a mechanism for shear-induced failure of loose
381 granular slopes, Can. Geotech. J., 51(5), 496–507, doi:10.1139/cgj-2012-0457, 2014.
382 Zhang, Y., Qi, M. and Ma, H.: Slope instability and its control in Shenzhen City, Chinese J. Rock Mech.
383 Eng., S2 (in Chinese), 2006.
384 Zou, D. H.: Exploring a Waste Dump Site Failure–Possible Causes and Prevention Measures, Int. J.
385 Geohazards Environ., 2(1), 25–33, 2016.
386